

Figure 31  
*Small compressed Argon core  
 achieved with low fill pressure (3  
 atm).*

## 2.C Calculations of the Wavelength Dependence of Absorption

One of the many advantages of using short wavelength radiation as a fusion driver is the increased collisional absorption expected. The laser radiation penetrates to higher densities where the plasma is more collisional and where collisional absorption (inverse bremsstrahlung) is more effective. In general, inverse bremsstrahlung is believed to be the dominant absorption mechanism at any wavelength at low laser irradiation intensities; as the intensity is increased, the plasma becomes hotter, and therefore less collisional, and the absorption decreases. (At still higher intensities the ponderomotive force of the laser steepens the density profile and resonant absorption becomes the dominant mechanism, but the absorption will then be only  $\sim 30\%$ , independent of wavelength.) The intensity point at which the absorption falls off from values near 100% is believed to increase strongly as the laser wavelength decreases; therefore, by using short wavelength laser radiation, a high absorption may in principle be achieved at much higher intensities. Additionally, the fraction of energy coupled into suprathermal electrons is simultaneously reduced.

SAGE is a two-dimensional hydrocode which has been under development at LLE over the last few years. The code is Eulerian, and uses an orthogonal grid with arbitrary mesh spacings in each direction. It supports planar, cylindrical, and spherical geometries, and may be run in one or two dimensions. Details of the code may be found in Reference 29.

The only absorption process modeled fully in SAGE is inverse bremsstrahlung (IB). In all the calculations described here, the laser radiation is incident normally upon the target, and a straight line approximation is used to describe the ray paths. This is a reasonable assumption, since two-dimensional calculations show that the critical surface never moves very far out from the initial target surface, and remains approximately parallel to its initial location, even for long pulses when the flow far from critical becomes divergent. Generally, most absorption occurs very close to critical even for long pulses because of the strong density dependence of the inverse bremsstrahlung coefficient:

$$K_{IB} = K_C \frac{(n_e/n_C)^2}{\sqrt{1 - n_e/n_C}} \quad (1)$$

In order to accurately calculate the IB absorption, SAGE makes use of analytic formula for the integral of  $K_{IB}$  within each cell. This procedure ensures good convergence with respect to zoning. For example, if the true spatial profile  $n_e(x)$  is exponential, SAGE will calculate the correct integral of  $K_{IB}$ , however coarse the zoning.

This picture may, however, not be so simple because it is generally accepted that for the intensities and laser pulse lengths of several nsec required for laser fusion, Brillouin instabilities in the underdense plasma may cause a substantial fraction of the incident laser energy to be reflected or scattered before it reaches the absorption region near the critical density. It is obviously imperative to understand how much energy can be coupled into the target under different circumstances for successful design of laser fusion targets. We have commenced by calculating the absorption for a wide variety of experimental conditions under the assumption of purely "classical" absorption physics, and we have obtained the surprising result that all of the fall-off of absorption at high intensities that has been observed in a wide range of recent experiments may be explained on the basis of this simple model, i.e. excluding such processes as Stimulated Brillouin Scattering (SBS). If our conclusion is correct, this is a significant and encouraging result.

In the sections below we describe the two-dimensional hydrocode SAGE, and calculations performed on SAGE to look at absorption and backscattering. For different irradiation geometries, laser pulsewidths and target materials, for four different laser wavelengths, and over several orders of magnitude of incident intensity, SAGE calculations are seen to be reasonably close to experimentally obtained results.

In addition, in the runs described below, SAGE dumps 15% of all energy reaching critical into a “non-thermal” electron distribution, as a Maxwellian described by a hot temperature  $T_H$  obtained from the local intensity according to the model of Reference 30. This purely ad hoc prescription provides a means of producing the supra-thermal electron component observed in many experiments and approximates the resonant absorption process which occurs at high intensities. When inverse bremsstrahlung is dominant, this additional energy source is insignificant because 15% of the energy reaching critical is a small quantity. When resonant absorption is dominant the 15% may be an underestimate, but this regime is not of great interest as the total absorption will then be small (<30%).

The key to an accurate calculation of IB absorption is the electron temperature  $T_e$  in the critical region, since

$$K_C \sim Z n_C T_e^{-3/2}. \quad (2)$$

As the temperature increases both  $K_C$  and the absorption,  $A$ , decrease,  $T_e$  is determined from the incident laser flux  $I$  by how effectively the absorbed energy is transported from the critical region to the ablation region, and may be estimated<sup>31</sup> by equating the absorbed energy flux ( $A I$ ) to a multiple  $f$  of the “free-streaming limit”:

$$A I = f (n_e k T_e) \sqrt{k T_e / m_e}. \quad (3)$$

SAGE, in common with other laser fusion hydrocodes, does not allow higher heat fluxes than that given on the right hand side of (3). The importance of the parameter  $f$  in modeling experimental data has been understood for some time<sup>32</sup>.

A simple scaling law for IB is easily obtainable from Equations 2 and 3. For a plasma of scalelength  $L$ , the absorption  $A$  is a function of  $K_C L$ , where  $K_C$  is  $K_{IB}$  evaluated at critical ( $n_C \propto \lambda^{-2}$ ) neglecting the square root term in Equation 1. Since

$$K_C L \sim Z n_C T_e^{-3/2} \times L \sim Z n_C (f n_C / I) \times L \sim Z f L / I \lambda^4,$$

we find that the absorption is a function of the quantity

$$Q = \frac{f Z L}{I \lambda^4}. \quad (4)$$

For example, tripling the laser frequency allows the same absorption to be obtained at an intensity  $3^4 = 81$  times greater, assuming that  $f$ ,  $Z$ , and  $L$  remain unchanged.

Care must be exercised in applying Equation 4 because  $L$  is an unknown quantity which may depend on any of the other parameters in the formula as well as on other quantities such as the pulse length and target geometry. A hydrocode is required to

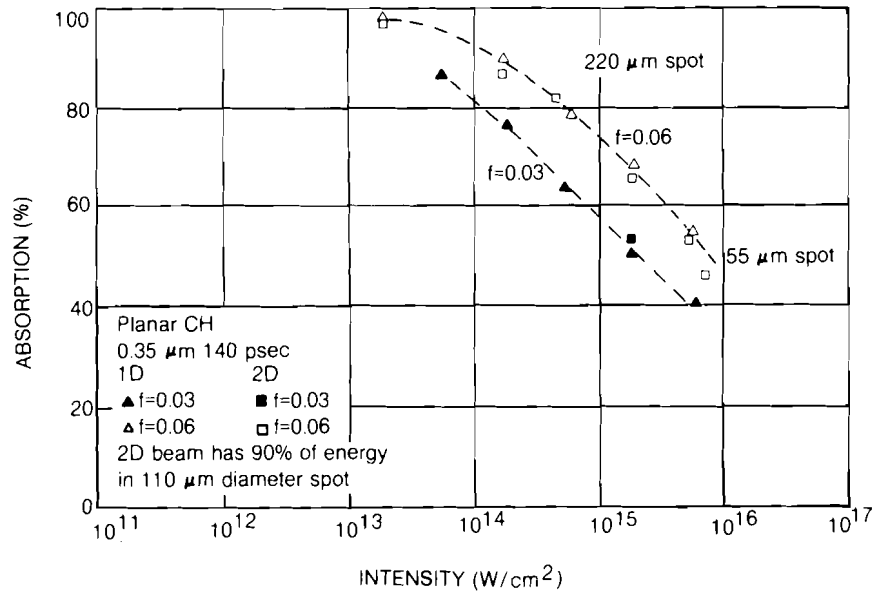


Figure 32  
 SAGE 1D and 2D calculations of  $A(I)$  for  $f=0.03$  and  $0.06$ , for 140 psec pulses of  $0.35\mu\text{m}$  radiation on planar CH targets.

Nominal intensity of Gaussian 2D beam must be defined as the power divided by the area containing 90% of the energy.

accurately calculate  $L$ . (For example,  $L$  may decrease as  $f$  is decreased, as  $Z$  increases, or at high intensities where ponderomotive steepening becomes important.) In addition, we are assuming that  $f$  is a basic physical quantity, independent of the other parameters, and this may not be correct although there is growing evidence that  $f$  varies very little.

SAGE also uses a tabular equation of state (SESAME<sup>33</sup>), which is important because it enables the code to treat spatially and temporally varying ionization states and the specific heat associated with ionization under the implicit assumption of local thermodynamic equilibrium. The LTE approximation is usually accepted to be valid over a wide range of laser intensities and pulse widths for low- to moderate- $Z$  materials, such as plastics, glass, etc. The energy deposited into the non-thermal electron distribution is treated by a multi-group flux-limited diffusion model (using typically 20 groups). The radiation emitted from the plasma is calculated from the Los Alamos Astrophysical Library tables<sup>34</sup>, and is transported by a similar multi-group diffusion model; typically 48 frequency groups are calculated.

Several physical effects are omitted from the calculations presented here. These include Stimulated Brillouin Scattering (SBS), magnetic field generation, non-LTE effects, ponderomotive steepening effects, and a high intensity inverse bremsstrahlung IB reduction factor<sup>35</sup>.

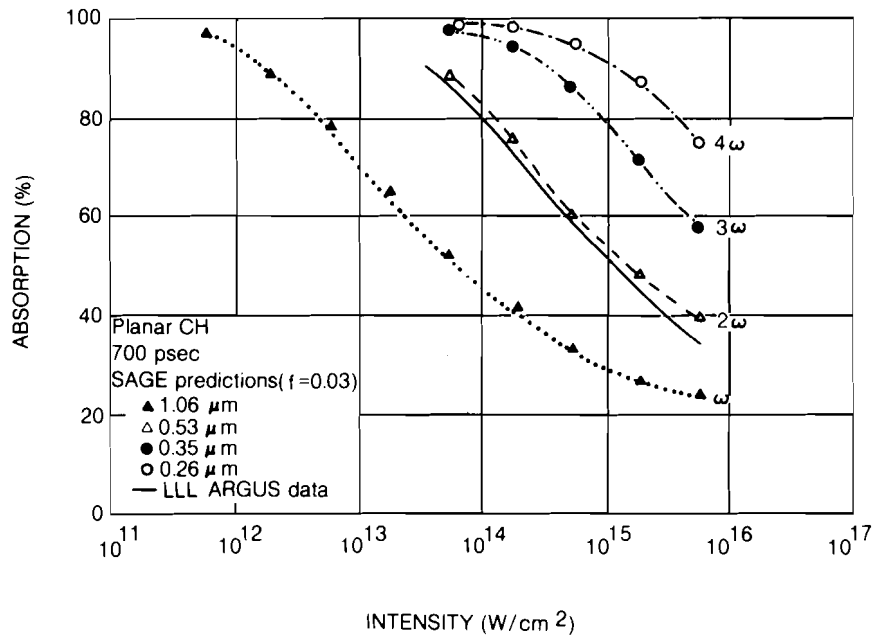


Figure 33  
 SAGE calculations of  $A(I)$  for  $f=0.03$ , for four different wavelengths, for 700 psec pulses and planar CH targets. The solid line is a fit to recent Livermore ARGUS data<sup>36</sup>.

Predictions for the absorption  $A$  versus intensity  $I$  are shown in Figure 32 for 140 psec Gaussian pulses at  $\lambda = 0.35 \mu\text{m}$  on planar CH. The two curves are for two values of the flux limit parameter ( $f = 0.03$  and  $0.06$ ). Notice the sensitivity to  $f$ : for  $I = 10^{15} \text{ W/cm}^2$ , the difference in  $A$  between the two cases is nearly 20%. The triangular points are for 1D planar calculations, and the square points are 2D calculations. The latter calculations use a spatially Gaussian radial beam profile whose nominal intensity is obtained by dividing the total power by the area containing 90% of the beam energy. (The normal intensity defined in this way provides a good estimate of the average intensity in the beam.) Two of the 2D calculations were performed using focal spots with respectively half and twice the radii of the other spots. The close correspondence between the 1D and 2D calculations suggests that to lowest order the absorption is not affected by 2D effects, allowing 1D planar runs to be used to map out the  $A(I)$  absorption characteristics.

Predictions for  $A(I)$  for the absorption on plastic at a few wavelengths of current interest are shown in Figure 33 for a 700 psec laser pulse and a flux-limit parameter  $f$  of 0.03. The solid line represents recent (preliminary) data from Livermore<sup>36</sup>, with error bars omitted. The slightly higher theoretical value near  $I = 10^{16} \text{ W/cm}^2$  may be due to the 15% dump at critical being unrealistically high for the long pulse length of the experiment; a better fit would probably be obtained with a slightly higher value of  $f$  and a "dump-all" fraction smaller than 15%. In any case, the close agreement is highly suggestive that no additional mechanism such as SBS is responsible for the fall-off of the absorption with intensity.

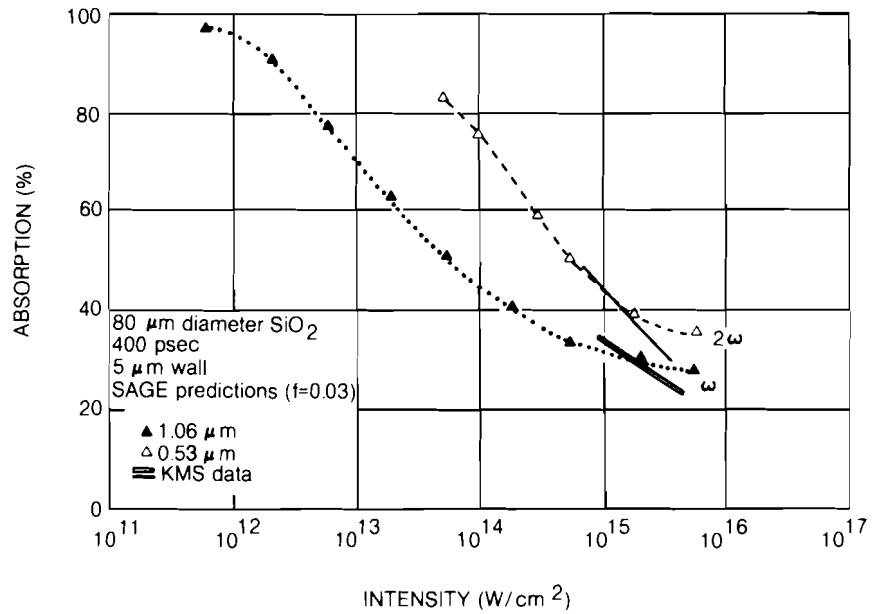


Figure 34  
 SAGE calculations of  $A(I)$  for  $f=0.03$ , for 400 psec pulses of  $1.06\mu\text{m}$  and  $0.53\mu\text{m}$  radiation on  $80\mu\text{m}$  diameter glass shells with  $5\mu\text{m}$  wall thickness. The solid lines are fits to recent KMS data<sup>37</sup>.

We do not preclude the possibility that SBS might occur very close to the critical surface<sup>41</sup>, when the scattered light would be subject to reabsorption in the plasma on its return path. In this case the total absorption would not be significantly degraded, although the small fraction “dumped” as resonant absorption would be reduced.

The  $I\lambda^4$  scaling suggested by Equation 4 is also (approximately) illustrated in Figure 33. For example, the intensity at which 80% absorption is obtained scales with wavelength approximately as  $I\lambda^{4.9}$ .

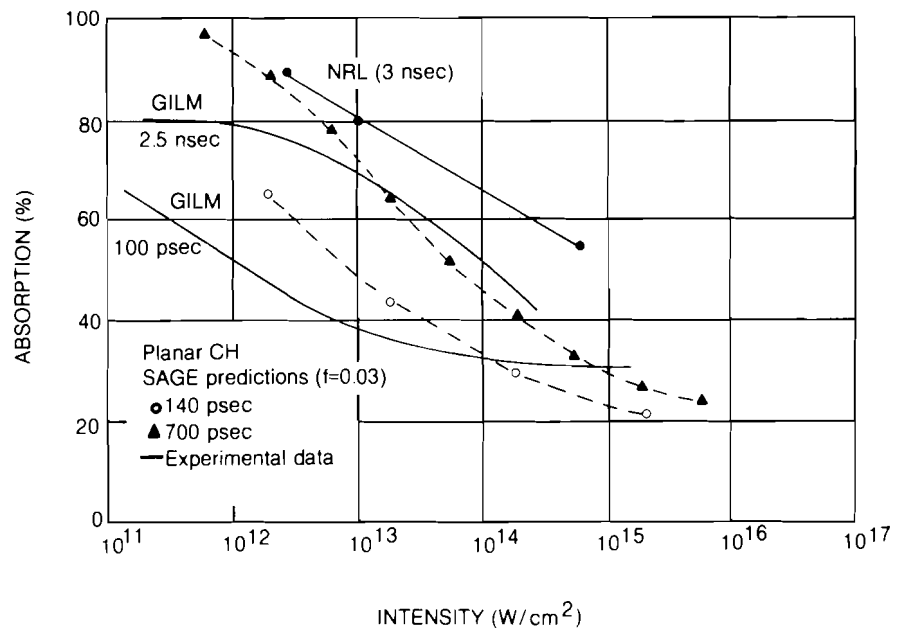


Figure 35  
 SAGE calculations of  $A(I)$  for  $f=0.03$ , for 140 and 700 psec pulses of  $1.06\mu\text{m}$  radiation and planar CH targets. The solid curves represent recent GILM<sup>38</sup> and NRL<sup>39</sup> data obtained under slightly different conditions.

In Figure 34, we plot SAGE predictions for 80 $\mu$ m diameter glass microballoons irradiated by 400 psec pulses (triangles), together with recent KMS data<sup>37</sup> obtained under very similar conditions (solid lines). The experimental errorbars on absorption are typically  $\pm 5\%$  at 0.53 $\mu$ m and less at 1.05 $\mu$ m. Here again the calculations use  $f = 0.03$ . The comparison is close for both wavelengths, but again the 15% dump gives a theoretical overestimate of the absorption for intensities greater than a few times  $10^{15}$  W/cm<sup>2</sup>. The slope of the 0.53 $\mu$ m data is again consistent with the fall-off in absorption being entirely due to IB, and we note that the numerical model of SBS used by Slater et al.<sup>37</sup> predicts very little reflection due to SBS under these conditions. Our predictions in the 1.06 $\mu$ m case at high intensities are closer to experiment than one would expect because of our exclusion of ponderomotive steepening; the continued fall-off of the experimental data in Figure 32 suggests that resonance absorption is not very important at these 400 psec pulse lengths even for 1.06 $\mu$ m irradiation.

In Figure 35 we plot SAGE predictions for planar CH targets, together with GILM<sup>38</sup> and NRL<sup>39</sup> results for short and long pulses. Here we have not used exactly the same pulsewidths and focal spot sizes as in the experiments, and exact comparison is therefore impossible. However, the trends are basically in agreement. For the short pulse GILM experiment it is likely that the 15% resonant absorption fraction is an underestimate. We do not understand at present what causes the difference between the GILM and NRL data at longer pulsewidths.

Considerable interest has been generated by Amiranoff et al.<sup>38</sup> who observed absorptions of over 90% on planar CH targets at

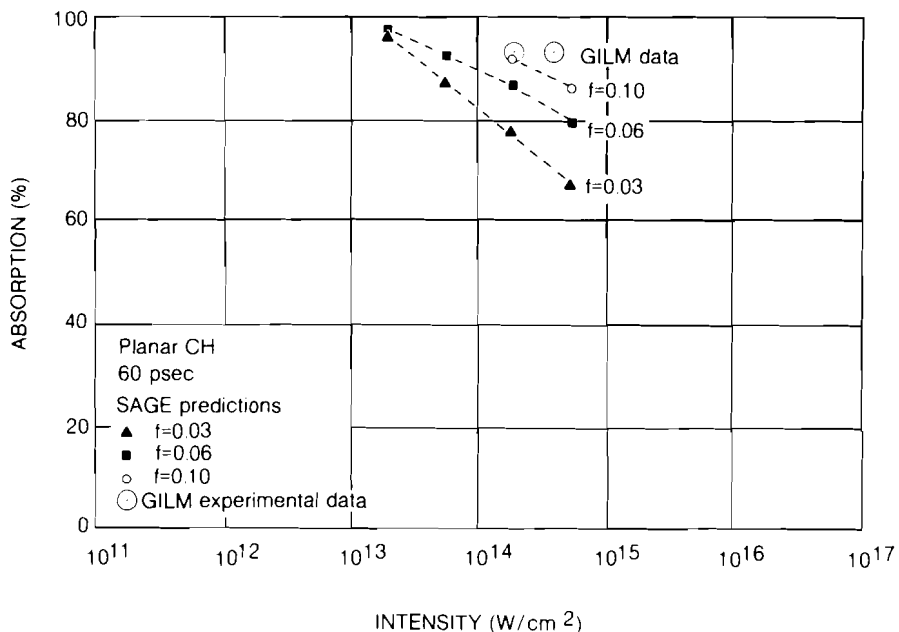


Figure 36  
 SAGE calculations of  $A(I)$  for 60 psec pulses of 0.26 $\mu$ m radiation on planar CH targets, for  $f=0.03$ , 0.06, and 0.10. Also shown are two recent GILM data points<sup>38</sup>

$I > 10^{14} \text{ W/cm}^2$  with  $0.26 \mu\text{m}$  radiation. These points, together with SAGE predictions for three different values of  $f$ , are shown in Figure 36. Here there is a definite discrepancy between theory and experiment, unless  $f$  is significantly greater than 0.03 in this case. Further experimental data, obtained over a broader intensity range, are clearly required.

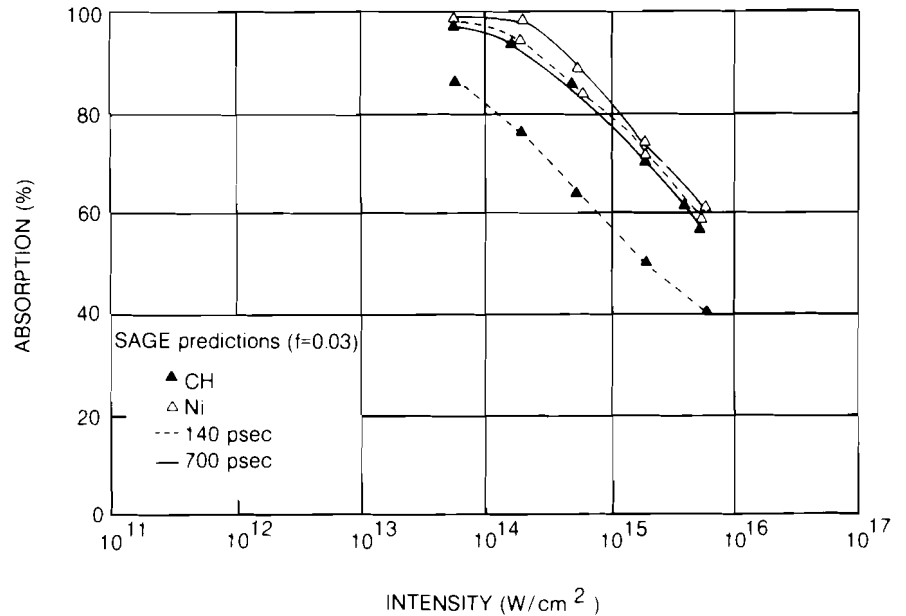


Figure 37  
SAGE calculations of  $A(I)$  for  $f=0.03$ , for 140 and 700 psec pulses of  $0.35 \mu\text{m}$  radiation on planar CH and Ni targets.

Finally, Figure 37 gives SAGE predictions for the absorption of  $0.35 \mu\text{m}$  light for plastic and nickel, for long (700 psec) and short (140 psec) pulses. Again, a value of 0.03 is used for  $f$ . The two lower curves (solid triangles) show that for plastic the absorption increases significantly at longer pulses. The two upper curves (open triangles) suggest a surprising result that for nickel ( $Z=28$ ) the absorption is almost independent of pulsewidth. This is believed to be due to a substantial steepening of the density profile near the critical density (induced by the low flux-limit parameter and not by ponderomotive forces which are not modeled).

It has recently been shown<sup>40</sup> that to correctly calculate the Doppler shift from a laser plasma two terms are involved, namely a shift ( $2V_c/c$ ) associated with the velocity of the critical surface and an additional shift due to the change of plasma density  $n_e$  (and therefore refractive index  $\mu$ ) in the underdense region. The total shift is given by the rate of change of the total optical path-length:

$$\begin{aligned} \frac{\Delta\lambda}{\lambda} &= \frac{d}{dt} \int \frac{\mu(x)dx}{c} \\ &= \frac{d}{dt} 2 \int_{x_c}^{\infty} \frac{1}{c} \sqrt{1 - n_e(x)/n_c} dx. \quad (5) \end{aligned}$$

$I > 10^{14} \text{ W/cm}^2$  with  $0.26\mu\text{m}$  radiation. These points, together with SAGE predictions for three different values of  $f$ , are shown in Figure 36. Here there is a definite discrepancy between theory and experiment, unless  $f$  is significantly greater than 0.03 in this case. Further experimental data, obtained over a broader intensity range, are clearly required.

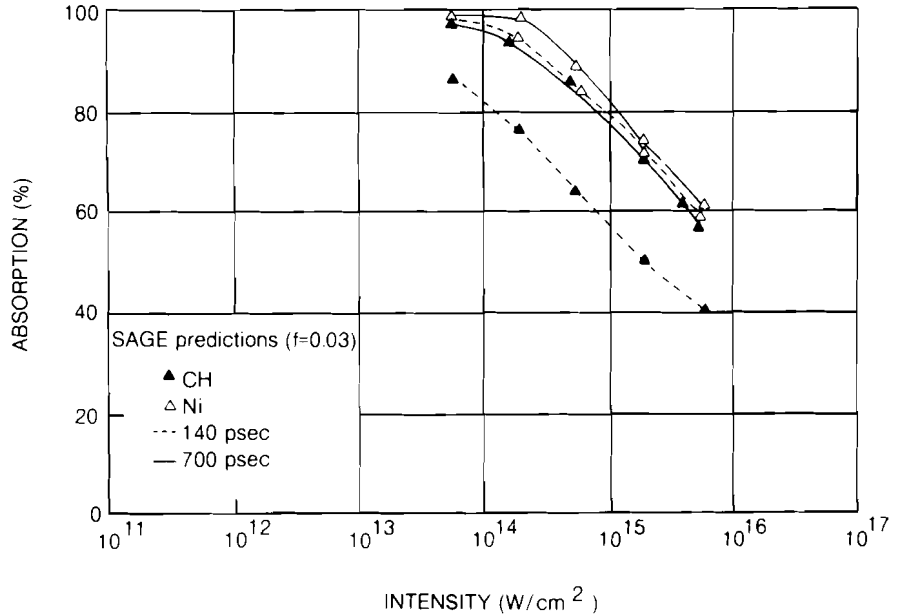


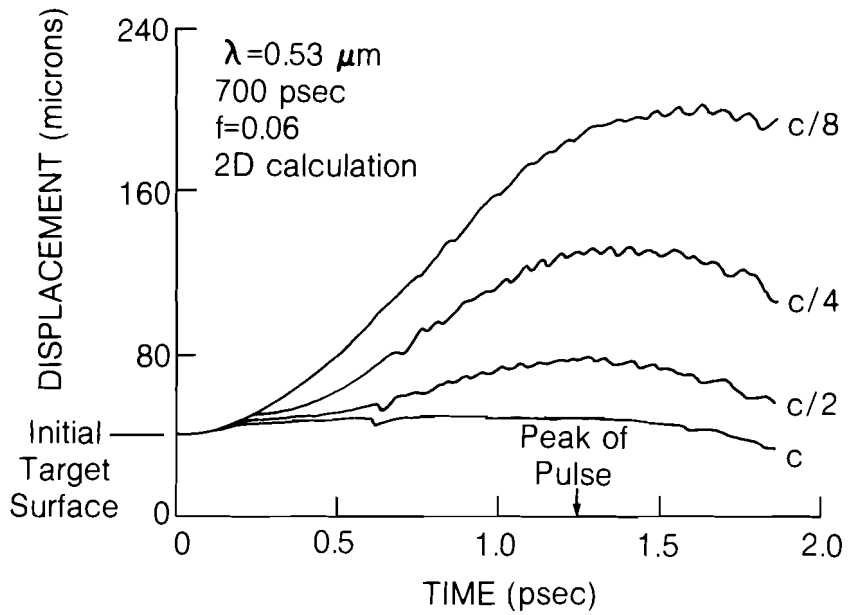
Figure 37  
SAGE calculations of  $A(I)$  for  $f=0.03$ , for 140 and 700 psec pulses of  $0.35\mu\text{m}$  radiation on planar CH and Ni targets.

Finally, Figure 37 gives SAGE predictions for the absorption of  $0.35\mu\text{m}$  light for plastic and nickel, for long (700 psec) and short (140 psec) pulses. Again, a value of 0.03 is used for  $f$ . The two lower curves (solid triangles) show that for plastic the absorption increases significantly at longer pulses. The two upper curves (open triangles) suggest a surprising result that for nickel ( $Z=28$ ) the absorption is almost independent of pulsewidth. This is believed to be due to a substantial steepening of the density profile near the critical density (induced by the low flux-limit parameter and not by ponderomotive forces which are not modeled).

It has recently been shown<sup>40</sup> that to correctly calculate the Doppler shift from a laser plasma two terms are involved, namely a shift ( $2V_C/c$ ) associated with the velocity of the critical surface and an additional shift due to the change of plasma density  $n_e$  (and therefore refractive index  $\mu$ ) in the underdense region. The total shift is given by the rate of change of the total optical path-length:

$$\begin{aligned} \frac{\Delta\lambda}{\lambda} &= \frac{d}{dt} \int \frac{\mu(x)dx}{c} \\ &= \frac{d}{dt} 2 \int_{x_C}^{\infty} \frac{1}{c} \sqrt{1 - n_e(x)/n_C} dx. \quad (5) \end{aligned}$$

Figure 38  
 Predictions for the time history of the critical, half-, quarter- and eighth-critical surfaces for a 40 μm thick CH slab irradiated by a 700 psec pulse of 0.53 μm radiation at 1.5 × 10<sup>14</sup> W/cm<sup>2</sup>. This calculation was performed in 2D.



For example, for an exponential profile  $n_e(x) = n_c \exp [(x_c - x)/L]$ ,

$$\frac{\Delta\lambda}{\lambda} = - \frac{2V_c}{c} - 1.23 \frac{dL/dt}{c} \quad (6)$$

SAGE calculates the full shift given by Equation 5 for rays which are assumed to be reflected normally from the plasma. Both terms have been found to be important. A similar model has recently been implemented by Tarvin and Schroeder<sup>42</sup>.

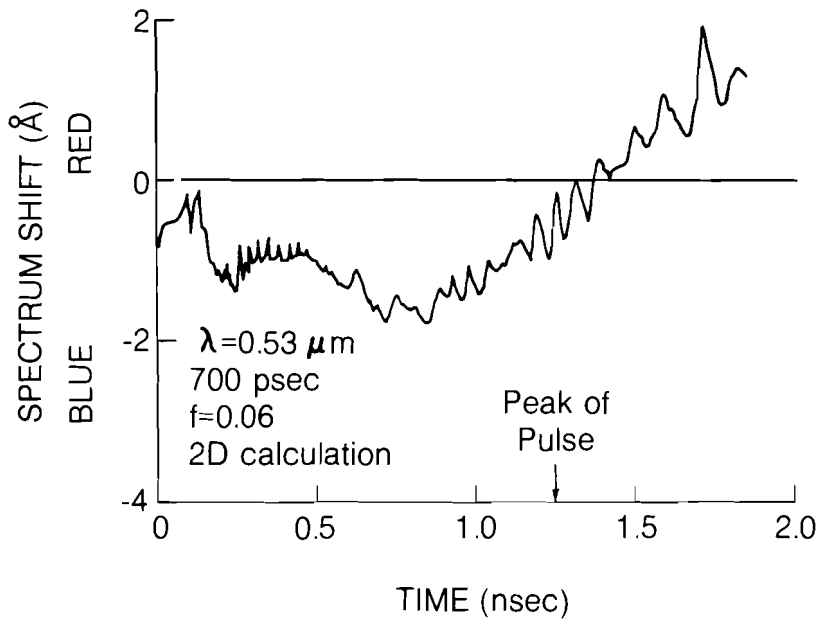


Figure 39  
 Predictions of the time history of the mean spectrum shift for the calculation of Figure 38.

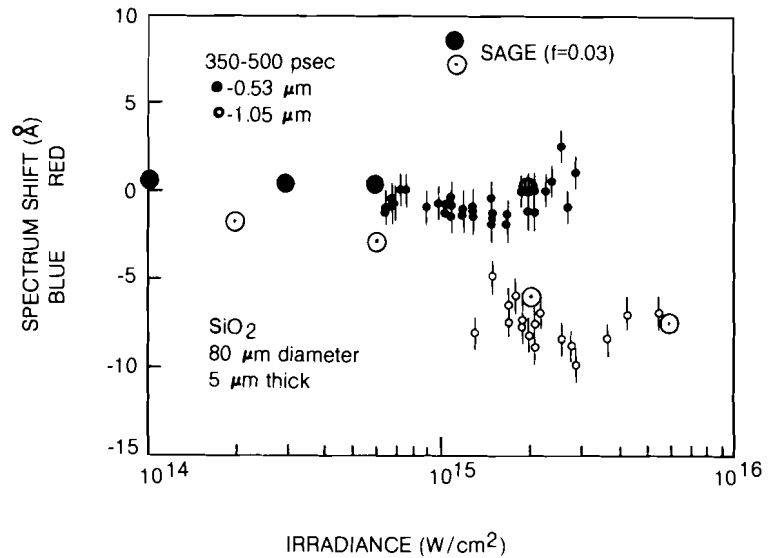


Figure 40

Predictions (circled points) for the time-integrated spectrum shift as a function of intensity, corresponding to the calculations of Figure 34, superposed on recent KMS experimental data<sup>37</sup>.

In Figure 38 trajectories for the (on-axis) critical, half-, quarter- and eighth-critical surfaces are plotted for a 2D calculation of  $0.53\mu\text{m}$  radiation incident upon a plastic target at  $1.5 \times 10^{14}$   $\text{W}/\text{cm}^2$ . (In this example  $f = 0.06$ , but the same qualitative behavior obtains for other values of  $f$ .) The ripples on the curves are numerical artifacts which should be ignored. The critical surface initially moves out very slowly, and then stays steady over most of the pulse. The underdense plasma lengthscale, as may be estimated from the half-critical trajectory, increases up to the peak of the pulse, giving a blue-shift, and decreases later, leading eventually to a red-shift. A time history of the spectrum shift for this case would be as shown in Figure 39, where again it is the overall trend which is important while the ripples should be ignored.

The centroid of the time-integrated spectrum may also be calculated, and in Figure 40 we plot SAGE predictions (using  $f = 0.03$ ) together with KMS experimental data<sup>37</sup> for 400 psec pulses. There is qualitative agreement in that there is no significant shift for  $\lambda = 0.53\mu\text{m}$ , but a significant blue-shift for  $\lambda = 1.06\mu\text{m}$ , varying weakly with intensity. The centroid shift is a difficult quantity to compare with experiment, as usually the width of the experimental spectrum is much greater than the shift<sup>36</sup>. The code does not predict this experimental broadening, which could be due to microscopic fluctuations in the plasma occurring on small time-scales or to possible SBS occurring very close to the critical surface as discussed above. However, it is arguable that the centroid shift represents the dominant average plasma motion. Even if the theory does not explain fully the backreflected spectrum, it is clear that an accurate calculation (and subtraction) of the Doppler shift must be made before drawing conclusions about SBS.

In summary, it has been shown that a large set of experimental absorption and backreflection data may be explained classically, in terms of "flux-limited" transport, without invoking additional physical processes such as Stimulated Brillouin Scattering. This does not show that these processes are unimportant<sup>41</sup>, but rather underscores the need for the design of careful absorption experiments which resolve the important scattering and absorption processes.